A Quantum State–Resolved Insertion Reaction: O(^{1}D) + $H_2(J = 0) \rightarrow$ OH($^2\Pi$, v, N) + H(^{2}S)

Xianghong Liu,[1] Jim J. Lin,[1] Steven Harich,[1] George C. Schatz,[2] Xueming Yang[1,3]*

The O(^{1}D) + $H_2 \rightarrow$ OH + H reaction, which proceeds mainly as an insertion reaction at a collisional energy of 1.3 kilocalories per mole, has been investigated with the high-resolution H atom Rydberg "tagging" time-of-flight technique and the quasiclassical trajectory (QCT) method. Quantum state–resolved differential cross sections were measured for this prototype reaction. Different rotationally-vibrationally excited OH products have markedly different angular distributions, whereas the total reaction products are roughly forward and backward symmetric. Theoretical results obtained from QCT calculations indicate that this reaction is dominated by the insertion mechanism, with a small contribution from the collinear abstraction mechanism through quantum tunneling.

The quantum-state distribution of a nascent chemical reaction product carries important information in a reactive scattering experiment. Information on the angular distribution of the reaction product is also crucial in developing a complete picture of the reaction dynamics (*1*). Quantum state–resolved differential cross section measurements provide the most detailed mechanistic information on a chemical reaction, but in practice these are extremely difficult to obtain. The few reactive scattering systems that have been studied with quantum-state resolution (*2–8*) have provided insight into direct abstraction reactions, in which one reactant removes an atom or functional group from another reactant, mainly by forming a new bond. However, insertion reaction mechanisms are also important. For example, the reaction of a carbene (:CH_2) insertion into the C-H bond plays a key role in carbon chain growth in organic chemical reactions (*9*), and the insertion of olefins into metal-to-carbon bonds and the insertion of C-O bonds are also believed to be important in catalytic processes (*10*).

The reaction of O(^{1}D) + H_2 plays an important role in atmospheric (*11*) and combustion chemistry (*12*). Extensive experimental and theoretical studies have been carried out to elucidate the dynamics of this reaction and its isotopic variants, as reviewed recently by Casavecchia [(*13*); see also (*14–21*)]. Recently, Liu and co-workers (*17–21*) have measured the excitation function and the differential cross sections at different collisional energies for the O(^{1}D) + HD reaction using Doppler-selected time-of-flight (TOF) methods. At low collision energies (<1.8 kcal/mol), the reaction mainly goes through an insertion pathway that shows roughly a forward-backward symmetric product angular distribution. At energies above 1.8 kcal/mol, however, an additional abstraction channel becomes more and more important. This abstraction reaction mechanism is likely caused by excited-state reactive surfaces (*20, 21*). The general agreement between theory and experiment is quite good, but some differences still exist, particularly concerning the role of excited states (*20, 21*). Because of the limited resolution of the above experiments, quantum state–specific information on the radical products (OH) was not derived for this reaction in these experimental studies, and thus the total vibrational state distribution of OH could not be measured accurately. We now report studies of O(^{1}D) + H_2 that have much higher kinetic energy resolution, enabling us to determine full quantum state–resolved results for a collision energy of 1.3 kcal/mol. Detailed comparisons are made with the results of quasiclassical trajectory (QCT) calculations, including the influence of excited-state reaction channels.

The O(^{1}D) + *para*-$H_2(J = 0) \rightarrow$ OH($^2\Pi$, v, N) + H(^{2}S) reaction (J, rotational quantum number of H_2; Π, electronic state symbol with electronic angular momentum $L = 1$; v, vibrational quantum number of OH, N, rota-

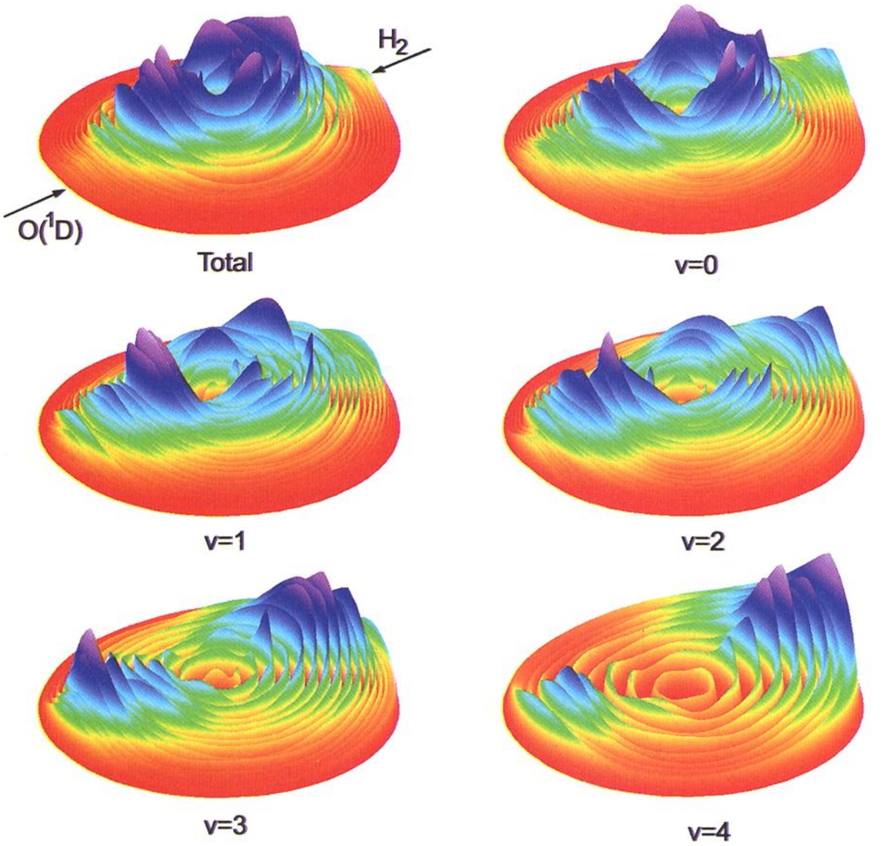

Total v=0 v=1 v=2 v=3 v=4

Fig. 1. Three-dimensional product contour plots for the total H atom products and the H products corresponding to the OH product from $v = 0$ to 4. Different layer structures correspond to the OH rotational structures in each individual v plot. The indicated arrows are the directions for the O(^{1}D) beam; the H_2 beam points to the opposite direction. The energetic limit for each plot is different.

---

[1]Institute of Atomic and Molecular Sciences, Academia Sinica, Taipei, Taiwan, ROC. [2]Department of Chemistry, Northwestern University, Evanston, IL 60208, USA. [3]Department of Chemistry, National Tsing-Hua University, Hsinchu, Taiwan, Republic of China.

*To whom correspondence should be addressed. E-mail: xmyang@po.iams.sinica.edu.tw

tional quantum number of OH) was studied with the high-resolution Rydberg "tagging" TOF technique pioneered by Welge and coworkers (*2, 3, 22, 23*). In this method, the H atom product is detected through a two-step excitation scheme to highly excited Rydberg states. The 121.6-nm vacuum ultraviolet (VUV) light used in the first step excitation is generated using a two-photon resonant ($2\omega_1$-ω_2) four-wave mixing scheme in a Kr/Ar gas cell (*24*). After the first-step VUV excitation, the H atom product is then sequentially excited to a high Rydberg state with $n \approx 50$ with 365-nm light (where n is the principal quantum number of the H atom). These two excitation laser beams must overlap exactly both in space and in time. The neutral Rydberg H atom then flies a certain distance for the TOF measurement and reaches a multichannel plate (MCP) detector with a fine metal grid (grounded) in the front. After passing through the grid, the Rydberg H atom products are then immediately field-ionized by the electric field applied between the front plate of the Z-stack MCP detector and the fine metal grid. The signal received by the MCP is then amplified by a fast preamplifier and counted by a multichannel scaler (MCS) (*23*).

We measured TOF spectra of the H atom products at 18 laboratory (LAB) angles (from 117.5° to –50° at about 10° interval). These TOF spectra were converted to the center-of-mass (CM) frame using a standard Jacobian transformation to obtain product kinetic energy (KE) distributions (*25*). The KE distributions obtained experimentally in the LAB frame were fitted by simply adjusting the relative populations of the rotational-vibrational (ro-vib) states of the OH product below the energetic limit for the reaction. From these fittings, relative population distributions of the OH product at each ro-vib state were determined at 18 different LAB angles. Quantum-state distributions of the OH product in the CM frame (Θ_{cm} = 0° to 180° at a 10° step) were then determined by a polynomial fit to the above results, and from these distributions, rotational state–resolved differential cross sections were determined. By incorporating all of the KE distributions in the CM frame, a three-dimensional (3D) contour plot of the differential cross sections in terms of CM angle and KE was easily constructed. Such 3D contour plots for the total H atom products and for the H atom products corresponding to each individual OH vibrational state are shown in Fig. 1. The angular distributions for the OH product at $v = 0$ to 4 were determined by integrating over all of the rotational-state populations for each vibrational level. The angular distributions for the OH products at $v = 0$ to 3 (Fig. 2A) appear to be roughly forward and backward symmetric, as was seen in previous experimental measurements in the total product angular distribution. Note, however, that the angular distribution for OH at $v = 4$ is clearly backward-scattered relative to the O(^{1}D) beam.

Although general features of the 3D product contour plots for different OH vibrational states are strikingly different from each other, some underlying features are similar. From the 3D contour plots for each OH vibrational state, the low rotationally excited OH products ($N < \sim10$) at all different vibrational states are mostly forward- or backward-scattered, whereas the angular distributions for highly rotationally excited OH products ($N > \sim10$) are more complicated. Generally, the angular distributions for the highly rotationally excited OH products are more isotropic and are sometimes strongly sideways-scattered. For the OH product at the individual ro-vib level, the angular distributions are not necessarily symmetric even though the overall OH angular distribution is roughly symmetric (see Fig. 1). The symmetric angular distribution of the total reaction product should result from the combined effect of the symmetry of the H_2O intermediate and its rotational randomization during the lifetime.

Total quantum-state distributions for this reaction can be determined by integrating these distributions over different CM angles. The OH rotational state distributions for each vibrational level are shown in Fig. 3. Such measurements were not possible previously because of problems associated with the laser-induced fluorescence (LIF) detection of OH (*26*). The distributions for different vibrational states are actually quite similar in that all distributions peak near their energetic limit (high J), indicating that the majority of the OH products from this reaction are significantly rotationally excited. By integrating the rotational distributions for each vibrational level, total OH product vibrational state distributions are also determined (Fig. 4). The population of the OH product at each vibrational level monotonically decreases as the vibrational energy increases.

To interpret the experimental results, we performed QCT calculations with the accurate ab initio surfaces of Dobbyn and Knowles (DK) (*27*). These surfaces include the ground-state (1A′) surface, which has the

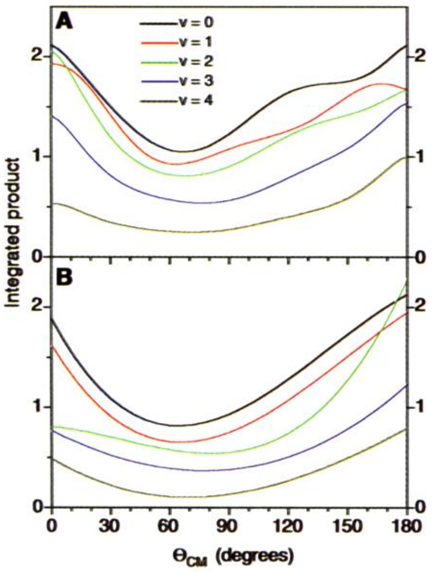

Fig. 2. Angular distributions for OH products at $v = 0$ to 4. (**A**) Experimental results. (**B**) Theoretical results based on QCT calculations on the DK surface.

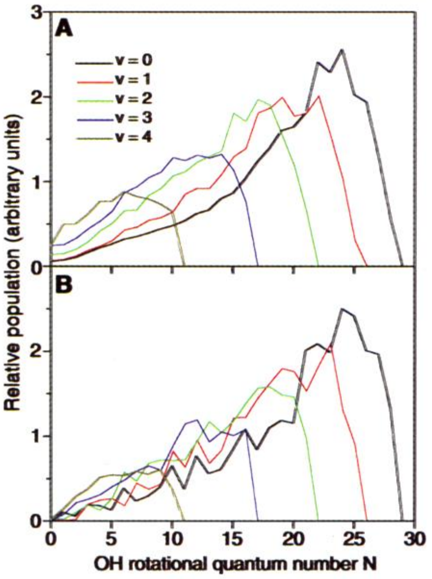

Fig. 3. Rotational distributions of the OH product at $v = 0$ to 4 for the reaction $O(^1D) + H_2(J = 0) \rightarrow OH(^2\Pi, v, N) + H(^2S)$ at 1.3 kcal/mol. (**A**) Experimental results. (**B**) Theoretical results based on QCT calculations on the DK surface.

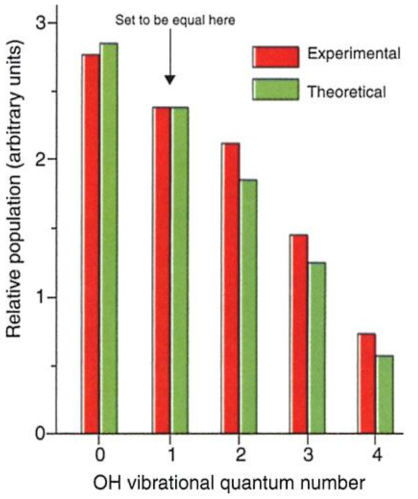

Fig. 4. Vibrational distributions of the OH product from the reaction $O(^1D) + H_2(J = 0) \rightarrow OH(^2\Pi, v, N) + H(^2S)$ at 1.3 kcal/mol. Theoretical results are based on QCT calculations on the DK surface.

perpendicular insertion pathway, and two excited states, 1A″ and 2A′, which have a collinear pathway with a 2.3 kcal/mol barrier. The 1A′ and 1A″ surfaces correlate to ground-state products and are not strongly influenced by nonadiabatic interactions (*28*). The 2A′ surface, by contrast, can only react via nonadiabatic coupling. Recently, Gray *et al.* used wave packets and trajectory surface hopping (TSH) calculations (*29*) to demonstrate that reaction can occur on 2A′ at low energies as a result of hopping from 2A′ to 1A′ at long range. In the present work, we have verified that these trajectories give the same product state and angular distributions as those that start on 1A′, and because the 2A′ cross section is small (~6% of 1A′), we have ignored its effect on the product distributions. In contrast, trajectories on the 1A″ surface yield product distributions that are typical for an abstraction reaction: Mostly low rotational states of $v = 3$ and 4 are populated, and backward-scattered angular distributions are seen. The QCT cross section on the 1A″ surface is negligible at 1.3 kcal/mol, but quantum scattering calculations (*29, 30*) find a small cross section due to tunneling that could, in fact, be detectable, especially if the ab initio barrier is slightly too high.

In the QCT results plotted in Figs. 2 to 4, we have included 1A′ results at 1.3 kcal/mol summed with 1A″ results that are based on a slightly higher energy (2.5 kcal/mol) and are multiplied by an empirical scale factor. The scale factor has been adjusted to fit the results for $v = 4$, $N = 4$ in Fig. 2, but this same factor also yields excellent agreement between theory and experiment in Figs. 2 to 4 (only $v = 3$ or 4 are affected by the 1A″ results). The ground-state total cross section is 81.3 atomic units, whereas the scaled 1A″ cross section is 2.6 atomic units. This 1A″ cross section is six times the size estimated from scattering calculations (*30, 31*), but a roughly 0.5 kcal/mol reduction in the barrier would account for the difference. This reduced barrier (1.8 kcal/mol) is also more consistent with that inferred from previous experimental studies (*18, 19*). The QCT results are overall in excellent agreement with experiment, and they demonstrate that most of the observed results are well described using the 1A′ surface. However, the $v = 3$ cross section has a 7% contribution from 1A″, and $v = 4$ has a 35% contribution, and this leads to noticeable backward scattering for these states.

Accurate quantum mechanical calculations on this system are desirable in order to develop a quantitative understanding of this reaction. Our experimental results should be able to provide a test ground for further theoretical studies of this benchmark insertion reaction at the full quantum dynamic level.

References and Notes

1. Y. T. Lee, *Science* **236**, 793 (1987).
2. L. Schnieder *et al.*, *Science* **269**, 207 (1995).
3. L. Schnieder *et al.*, *J. Chem. Phys.* **107**, 6175 (1997).
4. D. M. Neumark *et al.*, *J. Chem. Phys.* **82**, 3045 (1985).
5. D. M. Neumark *et al.*, *J. Chem. Phys.* **82**, 3067 (1985).
6. M. Faubel *et al.*, *Chem. Phys. Lett.* **232**, 197 (1995).
7. M. Faubel *et al.*, *J. Phys. Chem. A* **102**, 8695 (1998).
8. M. Baer *et al.*, *J. Chem. Phys.* **110**, 10231 (1999).
9. A. L. Ternay Jr., *Contemporary Organic Chemistry* (Sanders, Philadelphia, 1976), pp. 257–260.
10. B. E. Douglas, D. H. MacDaniel, J. J. Alexander, *Concepts and Models of Inorganic Chemistry* (Wiley, New York, ed. 2, 1983), pp. 461–478.
11. G. Anderson, *Annu. Rev. Phys. Chem.* **38**, 489 (1987).
12. G. Dixon-Lewis and D. J. Williams, *Compr. Chem. Kinet.* **17**, 1 (1977).
13. P. Casavecchia, *Rep. Prog. Phys.* **63**, 355 (2000).
14. T. Peng *et al.*, *Chem. Phys. Lett.* **248**, 37 (1996).
15. M. Alagia *et al.*, *J. Chem. Phys.* **108**, 6698 (1998).
16. M. Ahmed, D. S. Peterka, A. G. Suits, *Chem. Phys. Lett.* **310**, 372 (1999).
17. D.-C. Che and K. Liu, *J. Chem. Phys.* **103**, 5164 (1995).
18. Y.-T. Hsu and K. Liu, *J. Chem. Phys.* **107**, 1664 (1997).
19. Y.-T. Hsu, J. H. Wang, K. Liu, *J. Chem. Phys.* **107**, 2351 (1997).
20. Y.-T. Hsu, K. Liu, L. A. Pederson, G. C. Schatz, *J. Chem. Phys.* **111**, 7921 (1999).
21. ———, *J. Chem. Phys.* **111**, 7931 (1999).
22. L. Schnieder *et al.*, *J. Chem. Phys.* **92**, 7027 (1990).
23. Two parallel molecular beams (*para*-H_2 and O_2) were generated with similar pulsed valves. The O(^{1}D) atom beam was produced by photolysis of O_2 with 157-nm laser light from an F_2 laser (Lambda Physik LPX 2101). The O(^{1}D) beam was then crossed at 90° with the H_2 molecular beam. The *para*-H_2 molecular beam was generated by expanding the H_2 sample through a pulsed nozzle, which was cooled to the liquid nitrogen temperatures (~78 K). The use of a cold nozzle helps reduce the uncertainties of the collisional energy by minimizing the beam velocity spread. A small aperture was used to define the O(^{1}D) beam between the O_2 and H_2 beams. The velocity of the O(^{1}D) beam has been measured to be 2050 m/s with a very narrow velocity distribution ($v/\Delta v > 50$), whereas the velocity of the liquid nitrogen–cooled *para*-H_2 beam is 1384 m/s with a speed ratio ($v/\Delta v$) of about 15. [Because *para*-H_2 is expanded under the liquid nitrogen temperature, H_2 molecules in the beam should be all in the $J = 0$ state (*2, 3*)].
24. J. P. Marangos *et al.*, *J. Opt. Soc. Am. B* **7**, 1254 (1990).
25. During the conversion, detection efficiencies of the H atom product at different LAB angles and different velocities were simulated and thus included in the conversion. For laboratory spectra and product KE distributions for selected angles, see *Science* Online (www.sciencemag.org/feature/data/1052165.shl).
26. D. W. Hwang, X. F. Yang, X. Yang, *J. Chem. Phys.* **110**, 4119 (1999).
27. A. J. Dobbyn and P. J. Knowles, *Faraday Discuss.* **110**, 247 (1998).
28. G. C. Schatz, L. A. Pederson, P. J. Kuntz, *Faraday Discuss.* **108**, 357 (1997).
29. S. K. Gray, C. Petrongolo, K. Drukker, G. C. Schatz, *J. Phys. Chem. A* **103**, 9448 (1999).
30. K. Drukker and G. C. Schatz, *J. Chem. Phys.* **111**, 2451 (1999).
31. S. K. Gray and G. G. Balint-Kurti, personal communication.
32. Supported by NSF grant CHE-9873892 (G.C.S.), the National Science Council and Academia Sinica, and the China Petroleum Company. We thank Y. T. Lee, K. Liu, S. K. Gray, and G. G. Balint-Kurti for insightful discussions.

12 May 2000; accepted 21 June 2000

---

^{92}Nb-^{92}Zr and the Early Differentiation History of Planetary Bodies

C. Münker,[1]* S. Weyer,[1] K. Mezger,[1] M. Rehkämper,[1] F. Wombacher,[1] A. Bischoff[2]

The niobium-92–zirconium-92 (^{92}Nb-^{92}Zr) extinct radioactive decay system (half-life of about 36 million years) can place new time constraints on early differentiation processes in the silicate portion of planets and meteorites. Zirconium isotope data show that Earth and the oldest lunar crust have the same relative abundances of ^{92}Zr as chondrites. ^{92}Zr deficits in calcium-aluminum–rich inclusions from the Allende meteorite constrain the minimum value for the initial ^{92}Nb/^{93}Nb ratio of the solar system to 0.001. The absence of ^{92}Zr anomalies in terrestrial and lunar samples indicates that large silicate reservoirs on Earth and the moon (such as a magma ocean residue, a depleted mantle, or a crust) formed more than 50 million years after the oldest meteorites formed.

Current knowledge about geologic and geochemical processes during the early history of Earth is mainly based on isotopic studies of meteorites and old crustal rocks that preserve ages of up to ~4.1 billion years ago (Ga) (*1, 2*). Studies of extinct radioactive decay systems are particularly useful for the study of processes that took place in the early solar system, because they provide better time resolution than long-lived chronometers. Recently, ^{182}Hf-^{182}W chronometry has been used as evidence that the segregation of Earth's core postdates the formation of the solar system by more than 50 million years

---

[1] Zentrallabor für Geochronologie, Mineralogisches Institut, Universität Münster, Corrensstrasse 24, 48149 Münster, Germany. [2] Institut für Planetologie, Universität Münster, Wilhelm Klemm Strasse 10, 48149 Münster, Germany.

*To whom correspondence should be addressed. E-mail: muenker@nwz.uni-muenster.de